

Supplementary material for “Origin of azimuthal seismic anisotropy in oceanic plates and mantle”

Thorsten W. Becker^{a,*}

^a*Department of Earth Sciences, University of Southern California, Los Angeles, CA*

Clinton P. Conrad^b

^b*University of Hawai'i at Manoa*

Andrew J. Schaeffer^c and Sergei Lebedev^c

^c*Dublin Institute for Advanced Studies*

* Address: Department of Earth Sciences, University of Southern California, MC 0740, 3651 Trousdale Pkwy, Los Angeles, CA 90089-0740, USA. Phone: ++1 (213) 740 8365, Fax: ++1 (213) 740 8801

Email address: twb@usc.edu (Thorsten W. Becker).

This supplementary material for “Origin of azimuthal seismic anisotropy in oceanic plates and mantle” by Becker et al. (*Earth and Planetary Sciences*, in press, 2014) contains additional details including, 1), a description of the construction of the azimuthally anisotropic tomography model *SL2013SVA*, 2), visualizations and quantitative cross-model comparisons between different azimuthally anisotropic models, 3), a table with the best fit, ridge-fixed reference frame *RNR* plate motion Euler poles, 4), a discussion of the *LPO* model in light of net rotation akin to Becker (2008), and, 5), depth-dependent model misfit plots akin to Figure 5 of the main text for alternative tomography models.

Description of model *SL2013SVA*

In this section, we provide a brief summary of the *SL2013SVA* model (the details of which are the subject of a forthcoming paper) as analyzed in the main text. For more details on our multimode waveform methods, we refer the interested reader to Lebedev et al. (2005), Lebedev and van der Hilst (2008), and Schaeffer and Lebedev (2013a). *SL2013SVA* is the anisotropic component of the model *SL2013SV* (Schaeffer and Lebedev, 2013a), with the isotropic and anisotropic components computed simultaneously using the same dataset of 521,705 successfully fit, vertical-component, broadband seismograms. These half-million seismograms were selected from a master dataset of more than 750,000, recorded by more than 3000 seismometers belonging to international, national, regional, and temporary networks running from the 1990s until 2012. A mutually consistent subset was selected using outlier analysis (selecting $\sim 522,000$ from 750,000, as outlined in Schaeffer and Lebedev, 2013a). The total period range spans 11–450 s.

The inversion procedure is split into three steps. First we apply the Automated Multimode Inversion (AMI; Lebedev et al., 2005) to a dataset of more than 5 million vertical-component seismograms, each of which has been pre-processed, quality-controlled, and response-corrected to displacement. The initial dataset includes seismograms from all earthquakes in the CMT catalog (e.g. Ekström et al., 2012), including relatively small events recorded at long distances; low signal to noise ratios are the main reasons for the rejection of many seismograms by the waveform inversion procedure. The result of a successful waveform inversion is a set of linear equations with uncorrelated uncertainties that describe one-dimensional (1D) average perturbations in *S*- and *P*-wave velocity within approximate sensitivity volumes between each source-receiver pair, with respect to a 3D reference model (Lebedev and van der Hilst, 2008). In the second step, the equations generated by AMI are combined together into one large system and solved for the 3D distribution of *P* and *S* velocities, and 2Ψ *S*-wave azimuthal anisotropy (eq. 1 of the main text), as a function of depth, spanning the crust, upper mantle, transition zone and the upper part of the lower mantle. The inversion is carried out subject to regularization, consisting of lateral smoothing and gradient damping, vertical gradient damping, and

a minor degree of norm damping. The third step consists of a final outlier analysis of the dataset, from which an additional $\sim 3.5\%$ of successful fits are removed *a posteriori*, leaving the most mutually consistent $\sim 511,000$ to be re-inverted for the final model.

SL2013SVA is parameterized laterally on a global triangular grid of knots (Wang and Dahlen, 1995) with an approximate inter-knot spacing of 280 km (same as *SL2013SV*). Vertically, the model is parameterized using triangular basis functions centered at 7, 20, 36, 56, 80, 110, 150, 200, 260, 330, 410, 485, 585, 660, 810, and 1009 km depth (with pairs of half triangles for the transition zone discontinuities). The lateral smoothing parameters are larger for anisotropic terms (compared to isotropic), however, the vertical gradient damping and norm damping are equal. Additionally, path re-weighting is incorporated in order to reduce the effect of the many similar paths in the dataset. In Figure S1 we present five slices through *SL2013SVA* (left panels, a–e) at 75, 125, 175, 225, and 275 km depth, with comparisons to *DR2012* and *YB13SV* in the center and right panels.

Several tests were performed to verify the quality and robustness of *SL2013SVA*. First, we examined inversions both with and without the inclusion of azimuthally anisotropic terms. Comparison of the resulting isotropic models are qualitatively identical (no change to the interpretation). Visually, the largest changes were in the depth range 50–150 km depth in the Pacific Ocean basin; the addition of anisotropic terms results in a reduction of small-scale isotropic heterogeneity. Quantitatively, the addition of anisotropy results in the largest change in isotropic RMS of 15 m/s, at 100 km depth. An even smaller change of ~ 10 m/s is observed at 150 and 200 km depth; at greater depths the isotropic RMS of both models is within 3–4 m/s ($< 0.1\%$ difference). Secondly, we tested the sensitivity to the chosen vertical gradient damping. Results demonstrate that the anisotropy orientations are largely insensitive to the degree of vertical gradient damping. Model *SL2013SVA2* as shown in Figure S2b, for example, has no vertical gradient damping and is correlated with *SL2013SVA* at the $r_{20} = 0.99$ level on average over the upper 350 km of the mantle.

Additional synthetic tests were carried out to ensure minimal cross-contamination between model parameters (*i.e.*, leakage of isotropic structure into anisotropic, and *vice versa*). Two synthetic datasets were generated through matrix multiplication of the design (“A”) matrix of *SL2013SVA* (and *SL2013SV*) with two different synthetic models: only the isotropic terms of *SL2013SV* (anisotropy set to zero) and only the anisotropic terms of *SL2013SVA* (isotropic set to zero). The synthetic datasets were inverted using the same parameters as those in the generation of *SL2013SVA* (and *SL2013SV*). Examination of the resulting models confirms the independence of the isotropic and anisotropic terms; $< 0.5\%$ azimuthal anisotropy amplitudes are observed with *SL2013SV* as input, and similarly $\sim 1\%$ maximum amplitudes in isotropic velocity for *SL2013SVA* as input.

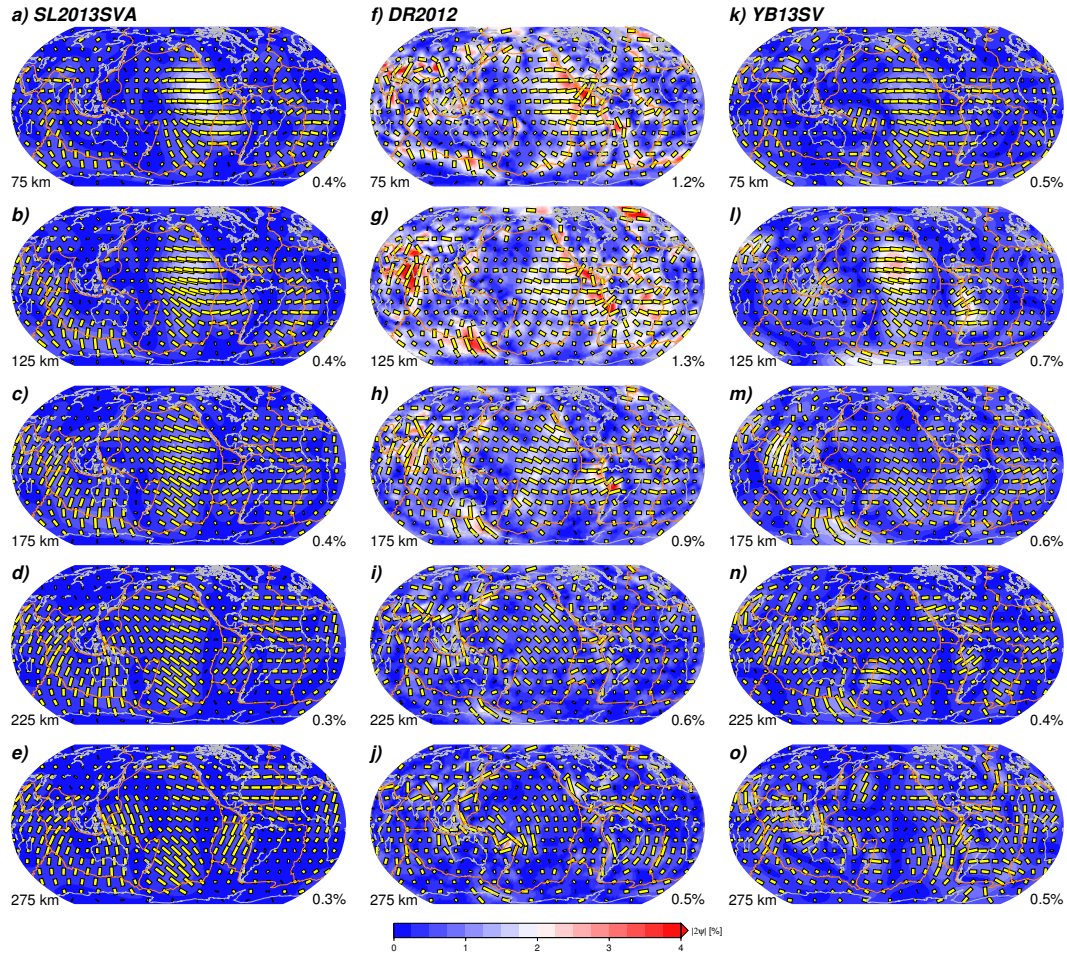


Fig. S1. Comparison of azimuthal anisotropy throughout the uppermost mantle from *SL2013SVA* (a-e, Schaeffer and Lebedev, 2013b), *DR2012* (f-j, Debayle and Ricard, 2013), and *YB13SV* (k-o, Yuan and Beghein, 2013), at the indicated depth levels. Sticks indicate the fast propagation orientation (Ψ), normalized to the maximum at each depth. Colored background indicates the amplitude of anisotropy, $|\Psi| = \sqrt{A_1^2 + A_2^2}$ (eq. 1 of the main text), with legend on lower right indicating the mean amplitude for each layer.

Radial correlation, cross-model correlation, and RMS of azimuthally anisotropic tomography models

We here provide some additional analysis of the character of the three different seismological models of upper mantle azimuthal anisotropy that were considered in the main text: *SL2013SVA* by Schaeffer and Lebedev (2013b) and as described above, *DR2012* by Debayle and Ricard (2013), and *YB13SV* by Yuan and Beghein (2013). The anisotropic patterns of these models are plotted for upper mantle depths in Figure S1. To further analyze the models, we expand the azimuthal anisotropy signal into generalized spherical harmonics as detailed in Becker et al. (2007).

We show radial correlation functions in Figure S2; those quantify the depth range

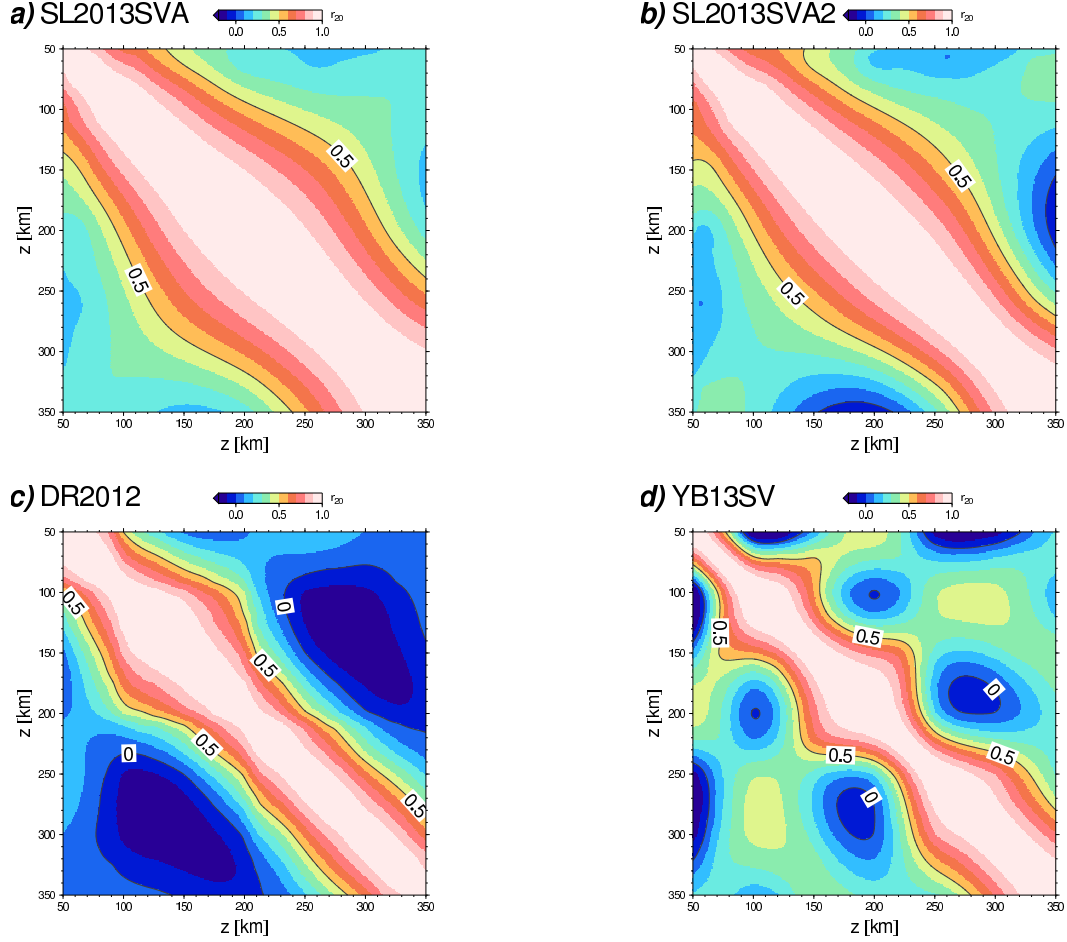


Fig. S2. Radial correlation functions for azimuthal anisotropy (2Ψ signal) of the three seismological models considered in the main text (a, c, and d; cf. Figure S1) based on generalized spherical harmonic expansion up to degree 20. Model *SL2013SVA2* is a test case using the same approach as in *SL2013SVA*, but applying no vertical damping.

over which structure is coherent, at each depth (e.g. Tackley et al., 1994; Puster and Jordan, 1997; Becker and Boschi, 2002). Figure S2 is based on total correlation up to degree L , r_L , with $L = 20$. It is clear that *SL2013SVA* is indeed very vertically smooth (by design), and *DR2012* lies intermediate between *SL2013SVA* and *YB13SV*, which allows for the most rapid variations of anisotropy with depth, as discussed by Yuan and Beghein (2013).

As *SL2013SVA* appears more vertically smooth than *DR2012* and *YB13SV*, we have conducted tests exploring the effect of the vertical gradient damping employed in generating *SL2013SVA*. A reduction in the vertical damping coefficients by several orders of magnitudes, compared to *SL2013SVA*, or even a complete removal of vertical smoothing, as for *SL2013SVA2* in Figure S2b, does not significantly affect the patterns of fast azimuths, which remain nearly unchanged at each depth, while the amplitudes are somewhat enhanced. We therefore think that the analysis presented in the main text is not adversely affected by undue structure due to smoothing.

Figure S3 explores the similarity in terms of anomaly patterns for the three seismological models. We compute cross-correlation, r_L , as a function of depth, depth-averages thereof, $\langle r_L \rangle$, and the RMS power. As was discussed by Becker et al. (2007) for phase velocity maps of azimuthal anisotropy, there are quite large differences in amplitude and patterns between models. That said, compared to the earlier analysis of phase velocity similarity, the newer 2Ψ models show $\langle r_3 \rangle$ correlation values that are larger than the old ones by ~ 0.2 , though still not close to the similarity of imaged isotropic SV structure, as expected. While all models agree in that most azimuthal anisotropy is focused in the upper ~ 350 km of the mantle, actual amplitudes of $|2\Psi|$ are still different by factors of ~ 5 in some depth ranges, and there are no consistent finer detail variations of RMS with depth, as expected from Figure S2.

However, as noted in the main text, it appears that the model on which we focus here, *SL2013SVA*, is more similar to the other two models, *DR2012* and *YB13SV* than they are to each other, based on the pattern match shown by average cross correlations. This might indicate that *SL2013SVA*, which is quite smooth compared to the other models (cf. Figure S1), captures the long wavelength structure of average anisotropy well, even if finer-scale structure, such as rapid changes of anisotropy with depth (Figure S2, cf. Yuan and Beghein, 2013) are less well resolved by Schaeffer and Lebedev’s (2013b) model.

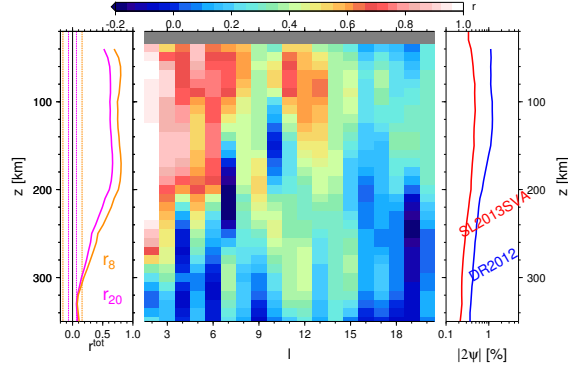
Best fit, ridge-fixed reference frame APM model *RNR*

For completeness, Table S1 provides the individual plate Euler poles for the *RNR* APM model we introduce in the main text based on minimizing the global motion of ridges. The model is identical to NUVEL-1A (DeMets et al., 1994) besides its net rotation component intended to minimize ridge motions, at a rate of $0.16^\circ/\text{Myr}$ with an Euler pole at $22^\circ\text{E}/82^\circ\text{S}$ relative to NNR.

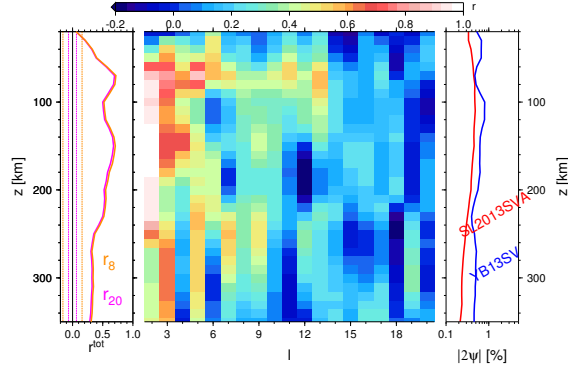
***LPO* model match as a function of net rotation**

Figure S4 reproduces the analysis of Becker (2008) (his Figure 2) for the more recent, azimuthally anisotropic tomographic models *SL2013SVA* (Schaeffer and Lebedev, 2013b), *DR2012* (Debayle and Ricard, 2013), and *YB13SV* (Yuan and Beghein, 2013) as considered in the main text. We show the match between tomography and *LPO* based on mantle flow computations that have varying degrees of net rotation of the lithosphere with respect to the lower mantle, from no net rotation (NNR) to the large net rotation found in HS3 (Gripp and Gordon, 2002). The metrics shown in Figure S4 are correlation, as computed for generalized spherical

a) SL2013SVA vs. DR2012, $\langle r_{20} \rangle = 0.45$, $\langle r_8 \rangle = 0.57$



b) SL2013SVA vs. YB13SV, $\langle r_{20} \rangle = 0.46$, $\langle r_8 \rangle = 0.48$



c) DR2012 vs. YB13SV, $\langle r_{20} \rangle = 0.26$, $\langle r_8 \rangle = 0.31$

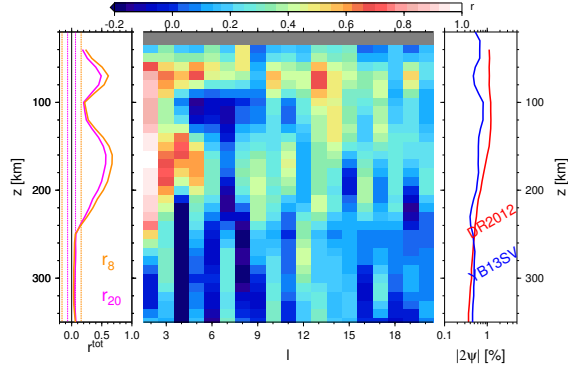


Fig. S3. Cross-model correlation and power for azimuthal anisotropy from seismology for uppermost mantle depths for the three models considered in the main text (cf. Figure S1). The 2Ψ signal has been expanded into generalized spherical harmonics (cf. Becker et al., 2007) up to degree $\ell_{max} = 20$. Left plot shows total correlation up to degrees $L = 8$ and 20 , r_8 and r_{20} , respectively, with depth, z (orange and magenta solid lines, with depth-averaged values, $\langle r_L \rangle$, given in the title), and the corresponding 95% confidence range from Student's t test (dashed lines). Center plot shows correlation as a function of ℓ and z , and rightmost plot shows the RMS heterogeneity on a log-scale.

Table S1

Euler vectors for each plate, $\vec{\omega}$, for the *RNR*, “ridge-fixed” APM model. The net rotation of this model with respect to NUVEL-1A (DeMets et al., 1994) in a no net rotation reference frame is $\vec{\omega}_{NR} = \{0.02056, 0.0083, -0.1583\}$, corresponding to 21.9451°E , 82.0136°S at a rate of $0.1599^\circ/\text{Myr}$; else, *RNR* is identical to *NNR* NUVEL1A. All Euler vectors are given in a $\{x, y, z\}$ Cartesian (East, North, Up) reference frame in units of $^\circ/\text{Myr}$.

<i>plate</i>	ω_x	ω_y	ω_z
Africa	0.0713	-0.1693	0.0663
Antarctica	-0.0268	-0.0892	0.0539
Arabia	0.4033	-0.0216	0.2289
Australia	0.4694	0.3019	0.2015
Caribbean	0.0100	-0.1857	-0.0679
Cocos	-0.5771	-1.2296	0.4675
Eurasian	-0.0360	-0.1289	0.0222
India	0.4024	0.0106	0.2306
Juan de Fuca	0.3067	0.4672	-0.4386
North America	0.0350	-0.1979	-0.1672
Nazca	-0.0675	-0.4831	0.3921
Pacific	-0.0663	0.2856	-0.7297
Philippine Sea	0.5983	-0.4020	-0.7297
South America	-0.0392	-0.0785	-0.2083

harmonics up to degree $\ell = 20$ (cf. Becker et al., 2007) and mean, angular orientational misfit, $\langle \Delta\alpha \rangle$, as in Figure 5 of the main text. The inferences drawn by Becker (2008) based on older azimuthal anisotropy models, that only moderate amounts of net rotation appear consistent with seismic anisotropy, are confirmed by the results in Figure S4.

Global depth dependence of geodynamic model misfit with azimuthal anisotropy for alternative tomography models

Figures S5 and S6 reproduce the global angular misfit as a function of depth plots discussed and presented in the main text for *SL2013SVA* (Schaeffer and Lebedev, 2013b) (Figure 5) for the alternative seismological models of azimuthal anisotropy from Debayle and Ricard (2013) (*DR2012*) and Yuan and Beghein (2013) (*YB13SV*).

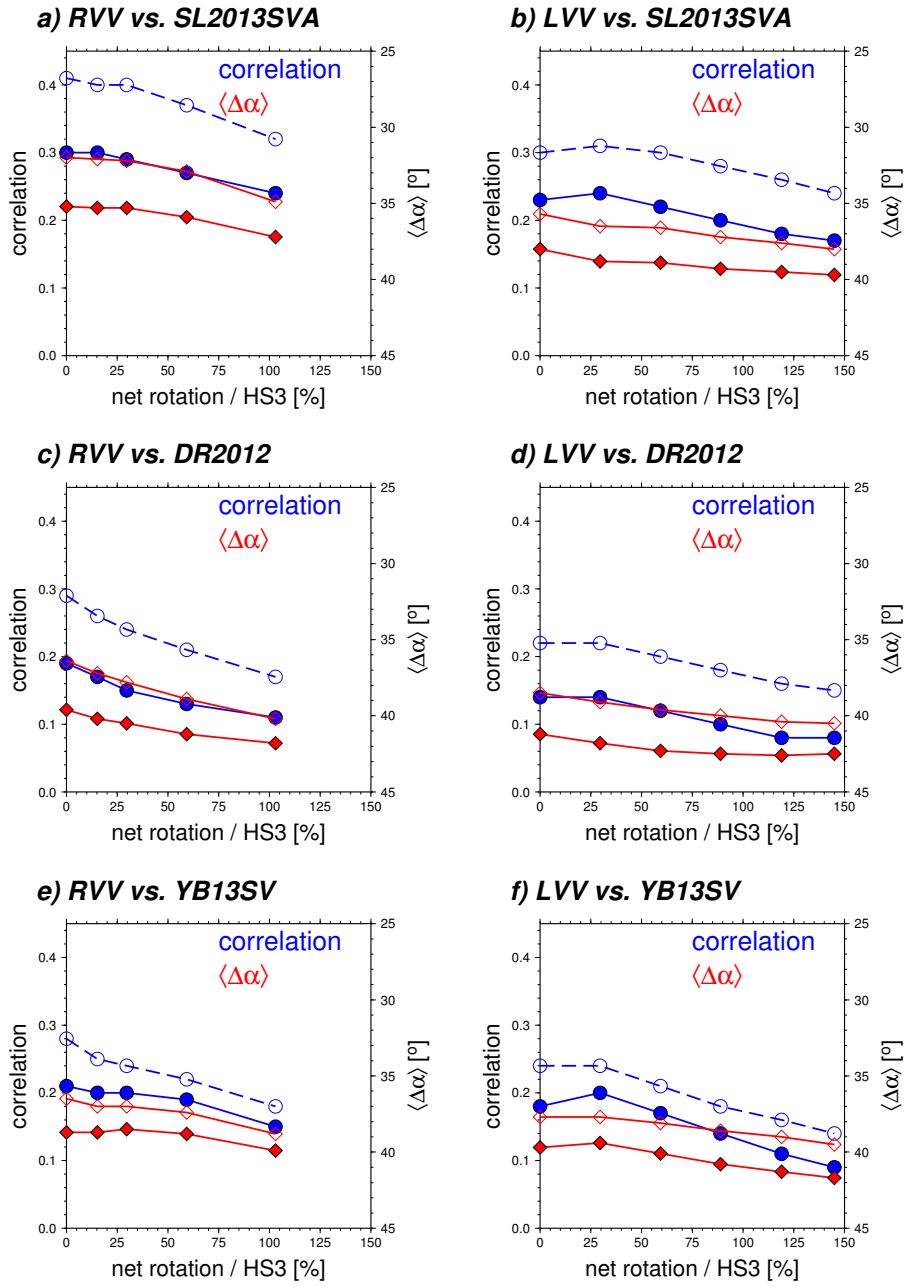


Fig. S4. Comparison of azimuthal anisotropy from tomography with *LPO* as predicted from mantle flow models with different degrees of net rotation of the lithosphere, expressed as fractions of HS3 (Gripp and Gordon, 2002). Results are from computations with only radial (a, c, e) and lateral viscosity variations (b, d, f), referenced to *SL2013SVA* (a, b), *DR2012* (c, d), and *YB13SV* (e, f). Solid and open symbols are for global metrics and when confined to oceanic plates only, respectively, and we show correlation computed from generalized spherical harmonics up to degree $\ell = 20$ and mean, angular orientational misfit, $\langle \Delta\alpha \rangle$. Figure is analogous to Figure 2 of Becker (2008), see there for details.

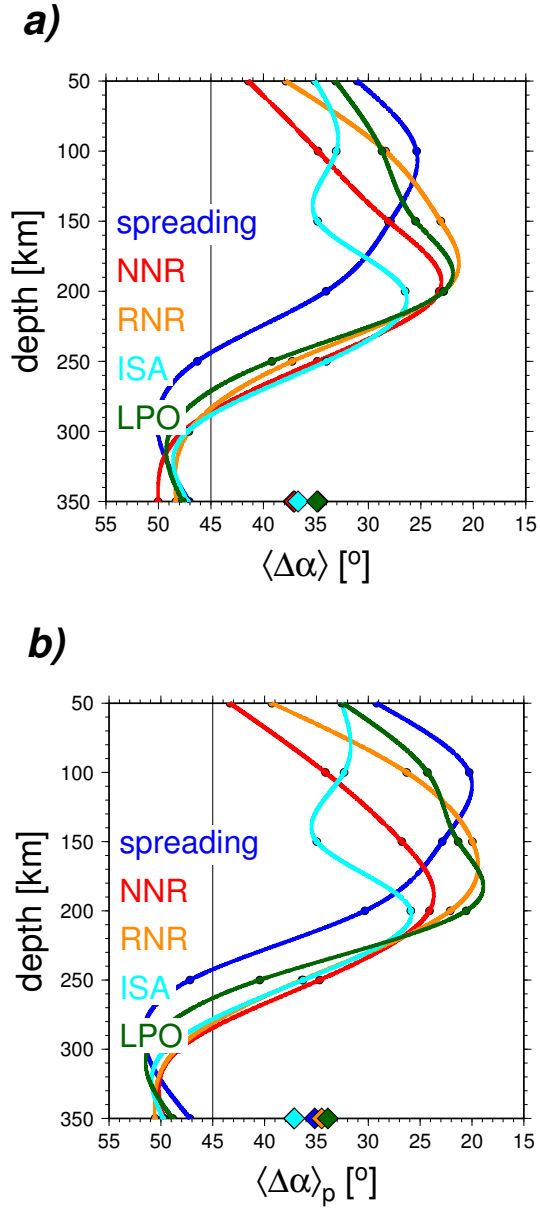


Fig. S5. a) Depth-dependence of global mean angular misfit, $\langle \Delta\alpha \rangle$, weighted by tomography anomaly amplitude, with azimuthal anisotropy in oceanic plates from *DR2012* (Debayle and Ricard, 2013) (see Figures 5 and S6 for other models). b) Depth dependence of misfit when computed weighing all oceanic basins evenly, $\langle \Delta\alpha \rangle_p$. Geodynamic models projected downward are paleo-spreading as well as APM models *NNR* and *RNR*. Depth-variable models based on mantle flow considered are *ISA* (Conrad and Behn, 2010) and *LPO* (Becker et al., 2008). Diamonds denote averages over the 50–350 km depth range for each model, as in Figure 5.

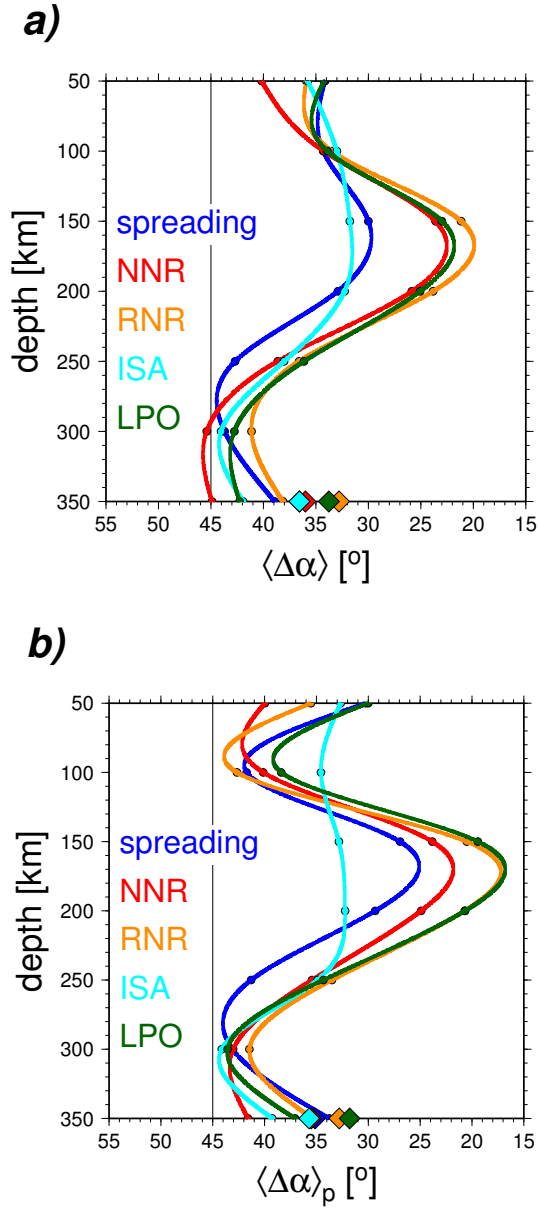


Fig. S6. a) Depth-dependence of global mean angular misfit, $\langle \Delta\alpha \rangle$, weighted by tomography anomaly amplitude, with azimuthal anisotropy in oceanic plates from *YB13SV* (Yuan and Beghein, 2013) (see Figure 5 and S5 for other models). b) Depth dependence of misfit when computed weighing all oceanic basins evenly, $\langle \Delta\alpha \rangle_p$. Geodynamic models projected downward are paleo-spreading as well as APM models *NNR* and *RNR*. Depth-variable models based on mantle flow considered are *ISA* (Conrad and Behn, 2010) and *LPO* (Becker et al., 2008). Diamonds denote averages over the 50–350 km depth range for each model, as in Figure 5.

References

- Becker, T. W., 2008. Azimuthal seismic anisotropy constrains net rotation of the lithosphere. *Geophys. Res. Lett.* 35, L05303. doi:10.1029/2007GL032928. Correction: doi:10.1029/2008GL033946.
- Becker, T. W., Boschi, L., 2002. A comparison of tomographic and geodynamic mantle models. *Geochem., Geophys., Geosys.* 3, 1. doi:10.1029/2001GC000168.
- Becker, T. W., Ekström, G., Boschi, L., Woodhouse, J. W., 2007. Length-scales, patterns, and origin of azimuthal seismic anisotropy in the upper mantle as mapped by Rayleigh waves. *Geophys. J. Int.* 171, 451–462.
- Becker, T. W., Kustowski, B., Ekström, G., 2008. Radial seismic anisotropy as a constraint for upper mantle rheology. *Earth Planet. Sci. Lett.* 267, 213–237.
- Conrad, C. P., Behn, M., 2010. Constraints on lithosphere net rotation and asthenospheric viscosity from global mantle flow models and seismic anisotropy. *Geochem., Geophys., Geosys.* 11, Q05W05. doi:10.1029/2009GC002970.
- Debaille, E., Ricard, Y., 2013. Seismic observations of large-scale deformation at the bottom of fast-moving plates. *Earth Planet. Sci. Lett.* 376, 165–177.
- DeMets, C., Gordon, R. G., Argus, D. F., Stein, S., 1994. Effect of recent revisions to the geomagnetic reversal time scale on estimates of current plate motions. *Geophys. Res. Lett.* 21, 2191–2194.
- Ekström, G., Nettles, M., Dziewóński, A. M., 2012. The global CMT project 2004–2010: Centroid-moment tensors for 13,017 earthquakes. *PEPI* 200–201, 1–9.
- Gripp, A. E., Gordon, R. G., 2002. Young tracks of hotspots and current plate velocities. *Geophys. J. Int.* 150, 321–361.
- Lebedev, S., Nolet, G., Meier, T., van der Hilst, R. D., 2005. Automated multimode inversion of surface and S waveforms. *Geophys. J. Int.* 162, 951–964.
- Lebedev, S., van der Hilst, R. D., 2008. Global upper-mantle tomography with the automated multimode inversion of surface and S-wave forms. *Geophys. J. Int.* 173, 505–518.
- Puster, P., Jordan, T. H., 1997. How stratified is mantle convection? *J. Geophys. Res.* 102, 7625–7646.
- Schaeffer, A., Lebedev, S., 2013a. Global shear speed structure of the upper mantle and transition zone. *Geophys. J. Int.* 194, 417–449.
- Schaeffer, A., Lebedev, S., 2013b. Global variations in azimuthal anisotropy of the Earth's upper mantle and crust (abstract). *Eos Trans. AGU*, DI11A–2172AGU Fall Meeting Abstract volume.
- Tackley, P. J., Stevenson, D. J., Glatzmaier, G. A., Schubert, G., 1994. Effects of multiple phase transitions in a three-dimensional spherical model of convection in Earth's mantle. *J. Geophys. Res.* 99, 15,877–15,901.
- Wang, Z., Dahlen, F. A., 1995. Spherical-spline parameterization of three-dimensional Earth models. *Geophys. Res. Lett.* 22, 3099–3102.
- Yuan, K., Beghein, C., 2013. Seismic anisotropy changes across upper mantle phase transitions. *Earth Planet. Sci. Lett.* 374, 132–144.